

Brief Report

# Pulmonary Nodule Detection and Classification Using All-Optical Deep Diffractive Neural Network

Junjie Shao <sup>1,†</sup>, Lingxiao Zhou <sup>1,†</sup> , Sze Yan Fion Yeung <sup>2</sup>, Ting Lei <sup>1</sup>, Wanlong Zhang <sup>1,\*</sup>  and Xiaocong Yuan <sup>1,3</sup>

<sup>1</sup> Nanophotonics Research Center, Institute of Microscale Optoelectronics, Shenzhen University, Shenzhen 518060, China

<sup>2</sup> State Key Laboratory on Advanced Displays and Optoelectronics Technologies, Department of Electronic & Computer Engineering, Hong Kong University of Science and Technology, Hong Kong SAR, China; eefion@ust.hk

<sup>3</sup> Research Center for Humanoid Sensing, Research Institute of Intelligent Sensing, Zhejiang Lab, Hangzhou 311100, China

\* Correspondence: zwl@szu.edu.cn; Tel.: +86-755-86950420

† These authors contributed equally to this work.

**Abstract:** A deep diffractive neural network (D2NN) is a fast optical computing structure that has been widely used in image classification, logical operations, and other fields. Computed tomography (CT) imaging is a reliable method for detecting and analyzing pulmonary nodules. In this paper, we propose using an all-optical D2NN for pulmonary nodule detection and classification based on CT imaging for lung cancer. The network was trained based on the LIDC-IDRI dataset, and the performance was evaluated on a test set. For pulmonary nodule detection, the existence of nodules scanned from CT images were estimated with two-class classification based on the network, achieving a recall rate of 91.08% from the test set. For pulmonary nodule classification, benign and malignant nodules were also classified with two-class classification with an accuracy of 76.77% and an area under the curve (AUC) value of 0.8292. Our numerical simulations show the possibility of using optical neural networks for fast medical image processing and aided diagnosis.

**Keywords:** pulmonary nodules; all optical; deep diffractive neural network; aided diagnosis; real time



**Citation:** Shao, J.; Zhou, L.; Yeung, S.Y.F.; Lei, T.; Zhang, W.; Yuan, X. Pulmonary Nodule Detection and Classification Using All-Optical Deep Diffractive Neural Network. *Life* **2023**, *13*, 1148. <https://doi.org/10.3390/life13051148>

Academic Editor: Yudong Cai

Received: 3 March 2023

Revised: 29 April 2023

Accepted: 7 May 2023

Published: 9 May 2023



**Copyright:** © 2023 by the authors. Licensee MDPI, Basel, Switzerland. This article is an open access article distributed under the terms and conditions of the Creative Commons Attribution (CC BY) license (<https://creativecommons.org/licenses/by/4.0/>).

## 1. Introduction

Artificial intelligence has become a highly researched and widely discussed topic in recent years. Deep neural networks have been utilized to solve various tasks such as natural language processing [1–3], image classification [4–6], object detection [7–10], semantic segmentation [11–13], etc. As the complexity and size of deep neural networks increase, more parameters need to be computed, which requires more time to process the input data. However, real-time processing tasks such as autonomous driving [14,15] are highly demanded, presenting a challenge to traditional parallel computing devices, e.g., graphics processing units (GPUs). Despite significant advantages in GPU technology in recent years, it is increasingly difficult to achieve further developments with silicon-based processing technology.

Optical neural networks represent a new and exciting direction in deep learning architecture, utilizing the propagation of light waves and modulation of the light field with optical devices to achieve ultra-fast computational speeds. Recent research has proposed various structures, including optical convolution networks [16,17], Mach–Zehnder interferometer-based optical networks [18–20], optical spiking neural networks [21,22], and diffractive deep neural networks (D2NNs) [23–37]. Due to D2NNs' simple structure with high parallel operation and low cost, there has been significant interest in D2NN research over the past few years, including increasing the networks' computation ability [24–29]

and robustness [30–32]. For instance, Li et al., proposed a differential diffractive network to enhance classification accuracy [24]. Zhou et al., used multiple photoelectric and electro-optic conversions to provide non-linear computation and improve the network’s inferential ability [26]. Moreover, various problems have been solved by D2NNs, such as image classification [23,33], filtering [34,35], logical operations [36,37], object detection [25,26], etc.

Medical imaging provides images of the human body’s internal organs. The image processing plays a crucial role in diagnosing various diseases. Computed tomography (CT) imaging is one of the best methods for detecting and analyzing pulmonary nodules. In recent years, deep learning has been applied to CT image analysis, including pulmonary nodule detection [38–40] and classification [39,41,42], demonstrating its effectiveness in this field. Experiments using D2NNs have been discussed in many research papers. Lin et al., reported that a 3D-printed optical diffractive layer can modulate a Terahertz light source and be composed into all-optical D2NNs, which were further applied for MNIST and Fashion-MNIST datasets [23]. Chen et al., presented optical diffractive units for visible wavelengths fabricated by a multi-step photolithography–etching method [43]. Luo et al., showed that the optical diffractive layers could be fabricated with a metasurface structure with 400 nm diffractive units to modulate visible light [44]. These studies demonstrated the feasibility of using all-optical networks in experiments.

In this paper, we propose the use of an all-optical D2NN for pulmonary nodule detection and classification to increase the speed of image processing and reduce waiting times for patients. The Lung Image Database Consortium image collection (LIDC-IDRI) dataset was used to train and test the network. In the numerical simulation, pulmonary nodule detection achieved a recall rate of 90.47% through the classification of whether pulmonary nodules existed or not. Using the trained all-optical network, slices of lung CT images were scanned to obtain information on the pulmonary nodules’ positions. For the pulmonary nodule classification, the network was adopted to classify benign and malignant nodules, achieving an accuracy of 76.77% and an area under the curve (AUC) of 0.8292, indicating the possibility of using all-optical neural networks in medical image processing. Furthermore, by combining the network with optical non-linear materials for advanced computation, the computing power and accuracy of the network can be further improved, indicating the possible uses of all-optical D2NNs in fast medical-image-aided diagnosis.

## 2. Methods

### 2.1. Dataset

The LIDC-IDRI dataset is a well-known database of thoracic CT scans and diagnostic results related to lung cancer [41,42]. In this dataset, 4 experienced thoracic radiologists analyzed the details of pulmonary nodules to classify them into 5 categories, with higher numbers indicating more serious nodules diagnosis. All the information were recorded in the XML files. In this work, the CT scans’ XML files were used to locate the pulmonary nodules and extract their diagnostic results.

### 2.2. All-Optical Diffractive Deep Neural Network

An all-optical D2NN is a novel approach that combines multiple optical diffractive layers, as illustrated in Figure 1. In this approach, the light field propagates in free space, and its phase and amplitude are modulated by a diffractive device, such as a spatial light modulator (SLM), liquid-crystal volume phase plates [45], or 3D-printed layers. According to the Huygens–Fresnel principle [46], the light field can be considered as many secondary wave sources, and the resulting propagation can be computed by the envelope influence of all secondary waves. The propagation of the secondary wave can be computed using scalar diffraction theory, such as the Rayleigh–Sommerfeld diffraction theory [46], and the impulse response can be expressed as:

$$w_i^l(x, y, z) = \frac{1}{2\pi} \frac{z - z_i}{r} \left( \frac{1}{r} - jk \right) \frac{\exp(jkr)}{r}, \quad (1)$$

where  $k = 2\pi/\lambda$  is the wave vector,  $\lambda$  is the wavelength,  $i$  refers to the  $i$ -th neurons in the  $l$ -th layer, and the distance between the current neuron and the  $i$ -th neuron in the  $l$ -th layer is given by  $r = \sqrt{(x - x_i)^2 + (y - y_i)^2 + (z - z_i)^2}$ . The imaginary unit is represented by  $j = \sqrt{-1}$ . The diffractive layer modulation can be expressed as  $t_i^l(x_i, y_i, z_i) = a_i^l(x_i, y_i, z_i) \exp(j\phi_i^l(x_i, y_i, z_i))$ , where  $a_i^l(x_i, y_i, z_i)$  and  $\phi_i^l(x_i, y_i, z_i)$  represent the amplitude and phase modulation factors, respectively. These factors are considered as trainable parameters in the neural network. The light field  $u_i^l(x_i, y_i, z_i)$  in the  $i$ -th neurons in the  $l$ -th layer can be express as:

$$u_i^l(x_i, y_i, z_i) = t_i^l(x_i, y_i, z_i) \cdot \sum_k u_k^{l-1} w_k^{l-1}, \tag{2}$$

The angular spectrum method used in training the networks describes light field propagation in Fourier space, reducing the operation time in the training section [46]. Thus, Equation (2) can be written as follows:

$$u_i^l(x_i, y_i, z_i) = t_i^l(x_i, y_i, z_i) \cdot \mathcal{F}^{-1} \left( U^{l-1}(u, v) \exp(j2\pi\gamma\Delta_z) \right), \tag{3}$$

where  $U^{l-1}(u, v) = \mathcal{F}(u^{l-1}(x, y, z))$  is the Fourier transform of the output light field in the  $(l - 1)$ -th layer,  $\Delta_z$  is the axial distance between the  $l$ -th layer and  $(l - 1)$ -th layer, and  $\gamma = \sqrt{1/\lambda^2 - u^2 - v^2}$ .

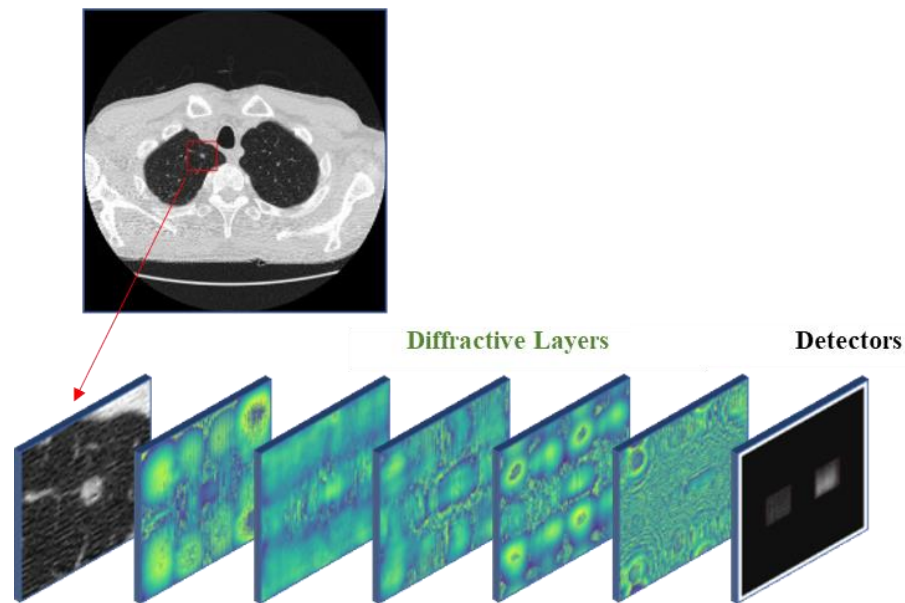


**Figure 1.** Schematic diagram of all-optical D2NN. The CT image, which serves as the input of the network, is clipped to a size of  $50 \times 50$  pixels (as shown in red square region) and modulated for the amplitude of the light field. The detectors at the designed positions record the intensity of the output field.

In this study, we investigated the feasibility of using visible light as the light source for the all-optical D2NN. The He-Ne laser with 632.8 nm wavelength was selected for the networks with 5 diffraction layers in our numerical experiments. The neuron distribution of the diffractive layers was set to  $200 \times 200$  (40,000 neurons per layer, and the size of each layer is  $0.8 \text{ mm} \times 0.8 \text{ mm}$ ) and  $400 \times 400$  (160,000 neurons per layer, and the size of each layer is  $1.6 \text{ mm} \times 1.6 \text{ mm}$ ) for detection and classification tasks, respectively. The axial distance between adjacent layers, including the detection plane, was set to 10 mm. Although the diffractive angle is not large enough to achieve full connectivity in the classification task [43], a sufficient number of neurons are obtained in the diffractive layers to modulate the secondary wave field created by the previous layer, and the networks still have a considerable number of trainable connections for training.

For our experiments, we clipped the CT images into  $50 \times 50$  pixels and resized them using nearest interpolation to  $200 \times 200$  pixels and  $400 \times 400$  pixels. In the training section, we set a batch size of 64 and the learning rates to 0.005 and 0.001 for pulmonary nodule detection and classification, respectively. The networks were trained for 120 epochs, and then we analyzed its inference performance on the blind test set. The results of the networks are indicated with the maximum intensity in the designed regions of the detecting plane, presenting the real-time computing results.

### 2.3. Pulmonary Nodule Detection

The network model was trained to detect the presence of nodules in CT images from the LIDC-IDRI dataset. Images were clipped around the center of each nodule and labeled as nodule regions, while images of the same size without nodules were also clipped and labeled as no-nodule regions. The number of images in both classes was balanced for training, and the dataset was divided into validation, test, and training sets in the ratio of 8:17:75.

During the training section, the propagated light amplitudes in 2 output detection regions were normalized by using  $A'_i = A_i / (A_0 + A_1 + b_0) + b_1$  ( $i = 0, 1$ ), where  $A_i$  is the sum amplitude of light field in the  $i$ -th detector, and  $b_0$  and  $b_1$  are 2 bias factors. The regions without nodules may have a large dark area, and the light intensity in detectors may be close to zero; thus, the factors  $b_0$  and  $b_1$  were applied in the normalization equation. The softmax cross-entropy loss was applied to optimize the network, as described in Equation (4) below [33]:

$$L_{crossentropy} = - \left[ A_0^{label} \log \left( \frac{\exp(A'_0)}{\exp(A'_0) + \exp(A'_1)} \right) + A_1^{label} \log \left( \frac{\exp(A'_1)}{\exp(A'_0) + \exp(A'_1)} \right) \right], \quad (4)$$

The networks were trained to classify nodules by scanning the entire CT image slices (see Figure 2). Equation (5) was applied to analyze the output of the network, obtaining the probability of nodules' existence as the score:

$$score = \frac{A'_i}{A'_0 + A'_1} \quad (i = 0, 1). \quad (5)$$

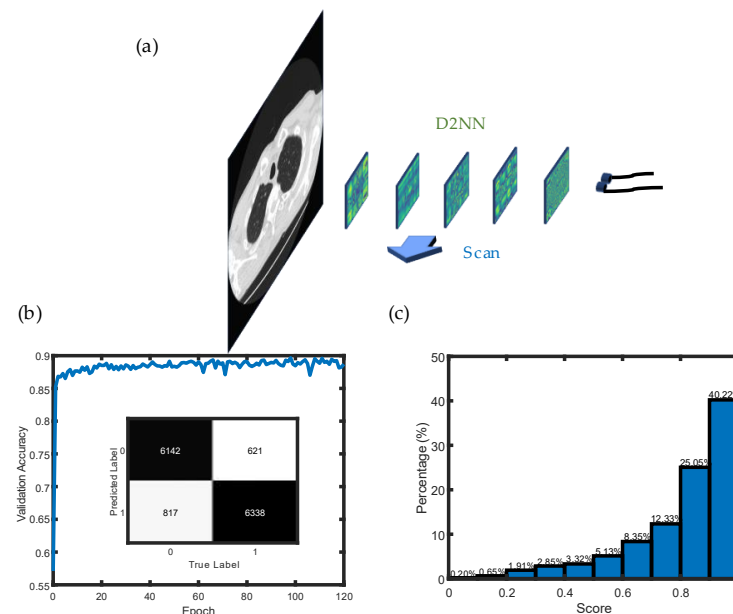


**Figure 2.** (a) Schematic diagram of scanning the slice of the CT image with the trained networks. (b) Training results of the networks and confusion matrix in test results. (c) Distribution of scores for nodules in the test set.

### 2.4. Pulmonary Nodule Classification

The location and classification of the nodules are provided in XML files, which divide the nodules into 5 classes (labeled 1–5). Benign nodules were labeled as “1” or “2”, while malignant nodules were labeled as “4” or “5”. Nodules labeled as “3” were discarded. To prepare the images for training, the images were clipped to a size of  $50 \times 50$  pixels, using the same method as mentioned in Section 2.3. The cases were also divided into validation, test, and training sets, with a ratio of 8:17:75, respectively. In addition, traditional data augmentation methods, such as rotating and flipping the images, were utilized to increase the number of images in the training set.

During the training process, the intensities of the 2 detectors in the output planes were also evaluated by using factor  $\alpha$ , as follows:

$$A'_i = \alpha \frac{A_i}{\max(A_0, A_1)} (i = 0, 1), \quad (6)$$

where  $A_0$  and  $A_1$  are the sum amplitudes in the 2 detectors' regions. The mean square error loss function (7) was applied to optimize the network as follows [23]:

$$L_{mse} = (A'_0 - \alpha A_0^{label})^2 + (A'_1 - \alpha A_1^{label})^2. \quad (7)$$

### 3. Results

Figure 2a,b present the training section of the networks and the accuracy of the network on the validation set converging after a few epochs, respectively. The detailed results are presented in the first two rows in Table 1. The networks' accuracy in the test set is 89.67% in the two-class classification, and the recall rate reaches 91.08%. The dataset can also be split into 10 parts with 10-fold cross validation, indicating that the mean accuracy in 10 folds is 89.72%, which is close to the performance in the test set. The score of each nodule in the test set was calculated to determine the existence possibility of the nodules. Figure 2c shows the distribution of scores, indicating that most nodules have a score higher than 0.7. In this case, the threshold of the score can be set higher than 0.5, and, at the same time, most of the regions can be detected with a correct result. The outputs of the networks were obtained from two detectors in the detection plane by comparing the amplitude of the light. In Figure 3a,b, the real-time inference results are shown, and the classification results can be clearly obtained by simply comparing the intensity in two detections directly.

**Table 1.** Nodule Detection Task Results in Validation and Test Sets.

| Work                                    | Accuracy (%) | Recall (Sensitivity) (%) | Precision (%) | F1 Score | MMC    |
|---|--------------|--------------------------|---------------|----------|--------|
| Trained with 1:1 ratio (validation set) | 89.54        | 90.96                    | 88.44         | 0.8968   | 0.7911 |
| Trained with 1:1 ratio (test set)       | 89.67        | 91.08                    | 88.58         | 0.8981   | 0.7937 |
| Trained with 1:4 ratio (validation set) | 92.67        | 69.66                    | 91.68         | 0.7917   | 0.7586 |
| Trained with 1:4 ratio (test set)       | 92.86        | 70.07                    | 79.68         | 0.7218   | 0.8585 |

MMC: Matthews Correlation Coefficient.

The trained networks were also applied to scan the CT image slices to search and detect nodules. The existence probability of the nodules was determined by the score of the clipped CT images, and a threshold was selected to assess the presence of nodules. Although there are many false-positive points in the results, almost all the nodules could be detected based on the networks' recall as shown in Figure 3c. Meanwhile, increasing the threshold can discard many false-positive points. However, the recall rate also reduced to 77.60% with a threshold of 0.7. Additionally, many regions without nodules are not included in the dataset, which also further influences the result. To balance the difference

ratio of images with and without nodules, the ratio was set to 1:4 to train and test the networks again. The training results and the confusion matrix are shown in Figure 4a, indicating the classification ability of the networks. The last two rows in Table 1 provide the detailed results of this trained network. The average accuracy in 10-fold cross validation is 92.49%, which is close to the accuracy in the test set (92.86%). The scan result is shown in Figure 4b, and the false-positive points are much less than before. However, the recall rate is also reduced to 70.07%, meaning that just 70.07% of the nodules are detected in the test set. In this case, both the threshold setting and the ratio of positive and negative samples influenced the result of the networks' performance.

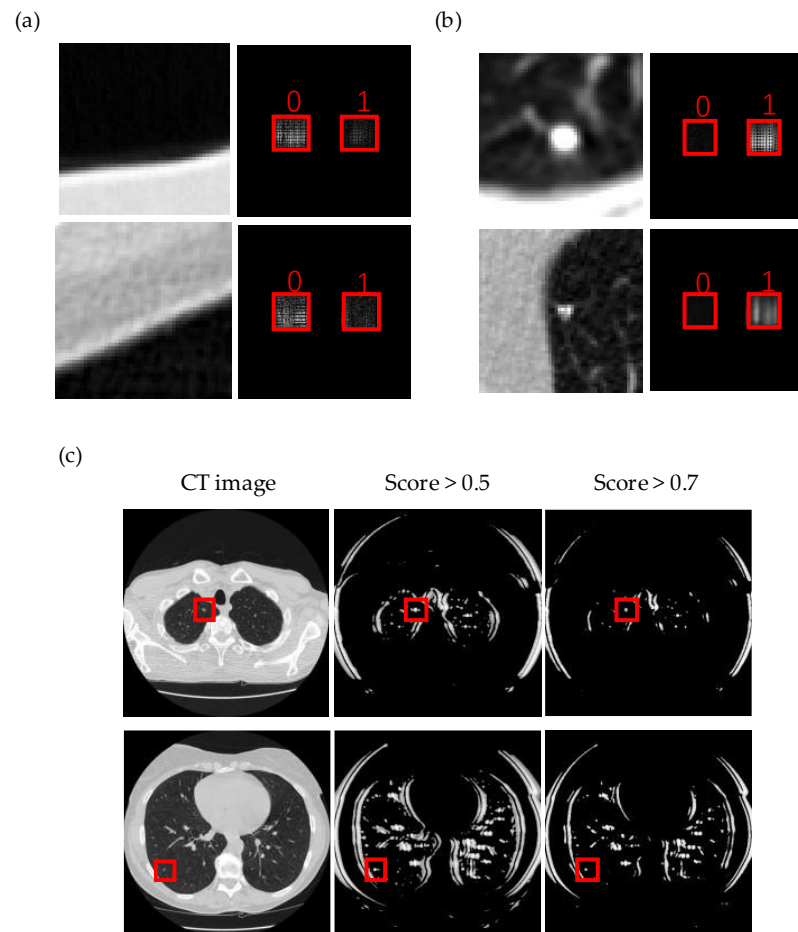


**Figure 3.** (a,b) Amplitude of the light field in forward inference results for negative and positive samples in the test set, respectively. The left image represents the input image, and the right image shows the amplitude of the light field in the two detectors' regions (as marked in red squares) in the output plane. The number "0" and "1" present the possibilities of negative and positive class, respectively. (c) Scan result of CT images. The white points on the images represent the regions that possibly have nodules, while the black points on the images represent the regions that have almost no nodules. The red square region shows the center of nodules in ground truth.

The networks were also used to classify nodules into benign and malignant categories. Figure 5a shows the training results, where the loss decreases quickly, and the network converges after a few epochs of training. Table 2 shows the performance of the trained network in the validation and test sets. The accuracy in the test set is 76.77%, and the recall rate reaches 65.97%, which is slightly different from that of the validation set. The reason may be that some difficult classified singular malignant nodules, were split in the validation set and there was not enough data to validate the performance of the trained network. Furthermore, 10-fold cross validation was performed, showing that the max accuracy reaches 79.43% with a mean accuracy of 74.59%. The confusion matrix and ROC

curve in the test set are shown in Figure 5b, with an AUC of 0.8292, indicating the credible classification result. The field distribution is shown in Figure 5c,d, when the images were inferred on the networks, with the left detector representing benign nodules and the right detector representing malignant nodules. The real-time output is the label of the region with the highest intensity.

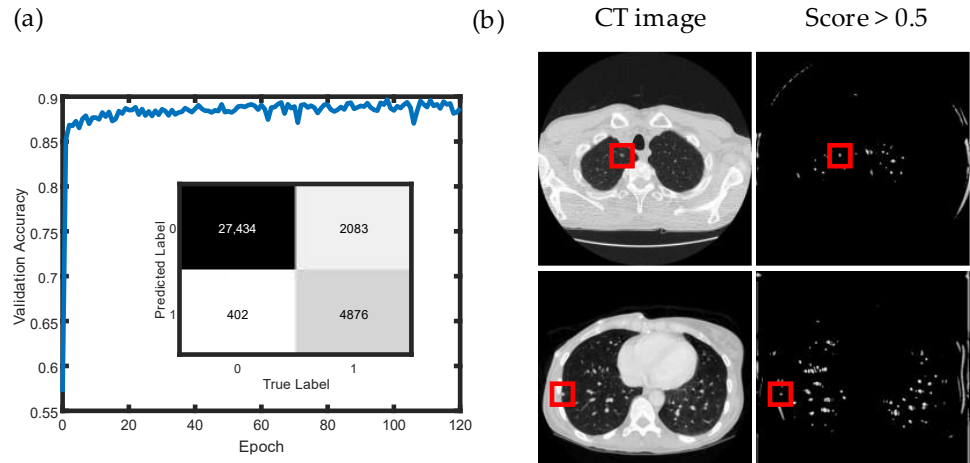


**Figure 4.** (a) Training section and confusion matrix in the test set of the dataset, whose ratio of nodules to non-nodules is 1:4. (b) Scan results of CT images. The white points on the images represent the regions that possibly have nodules, while the black points on the images represent the regions that have almost no nodules. The red square region shows the center of nodules in ground truth.

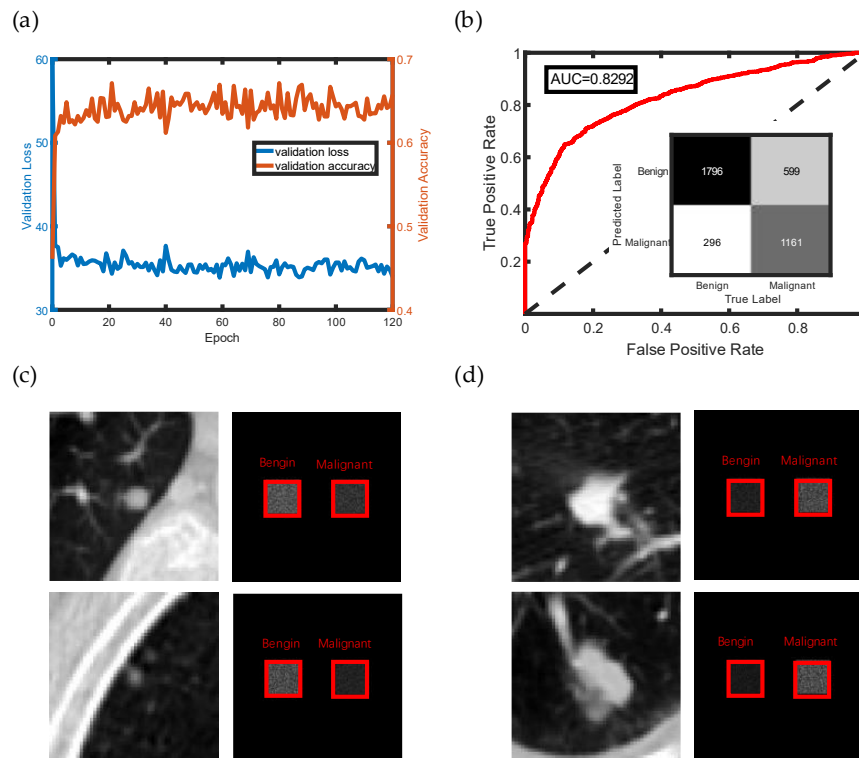


**Figure 5.** (a) Training results of nodule classification. (b) Confusion matrix and receiver operating characteristic (ROC) curve for the inference result in the test set. (c,d) Amplitude of the light field in forward inference of benign and malignant nodules, respectively. The left image represents the input image, and the right image shows the amplitude of two detectors' regions in the output plane.

**Table 2.** Nodule Classification Task Results in Validation and Test Sets.

| Work           | Accuracy (%) | Recall (Sensitivity) (%) | Precision (%) | F1 Score | MMC    |
|----------------|--------------|--------------------------|---------------|----------|--------|
| Validation set | 67.13        | 51.35                    | 77.08         | 0.6164   | 0.3706 |
| Test set       | 76.77        | 65.97                    | 79.68         | 0.7218   | 0.5323 |

MMC: Matthews Correlation Coefficient.

#### 4. Discussion

In this paper, we present the model of an all-optical deep diffractive neural network, which was trained and employed to perform nodule detection and classification tasks using the LIDC-IDRI dataset. The nodule detection task involved determining whether nodules were present or not, which was achieved with an accuracy of 87.78% and a recall rate of 90.47%. The trained networks were further used to scan CT image slices to detect nodules. Although the recall ratio in this study is similar to that of others, as shown in Table 3, it should be noted that traditional deep learning methods considered the whole size of CT images in the training section while our network only focuses on the partial section of CT images and considers only the centers of nodules as the targets. This explains why many false-positive points were detected in this study. Despite the performance of our all-optical network being slightly poorer than that of other computer-based methods, the classification of benign and malignant nodules achieved an accuracy of 76.77%, with an AUC of 0.8292, as shown in Table 4. The performance of the all-optical network could be improved by incorporating more non-linear computing sections. Overall, the simulation results demonstrate the potential of all-optical neural networks in real-time processing of medical images for aided diagnosis.

On the other hand, the network can be fabricated in experiments using optical devices, and its inference process can achieve speeds similar to light flight [23]. The network can be divided into three parts: the light source, optical diffractive layers, and detectors. The light source is the input of the network, while the optical diffractive layers modulate the light field to perform designed computation. The optical diffractive layers can be fabricated using a 3D-printed technique [23], multi-step photolithography–etching method [43], or metasurface technique [44]. The number of modulation units (trained parameters) does not affect the inference speed of the network, as the speed of light is constant. The detectors collect the final intensity of light, and once the input image is loaded, the distribution of light intensity can be directly seen at the detectors immediately, which represents the result of the network processing. Since the all-optical network has a forward inference speed similar to light, it has been reported in many fields [34–37,49–51].

**Table 3.** Comparison with Other Studies in Nodule Detection Task.

| Study                       | Recall (Sensitivity) (%) | Runtime   |
|-----------------------------|--------------------------|-----------|
| Ali et al. [38]             | 58.9                     | DPPU      |
| Harsono et al. [39]         | 94.12                    | DPPU      |
| Cao et al. [40]             | 92.5                     | DPPU      |
| Ours trained with 1:1 ratio | 91.08                    | Real time |
| Ours trained with 1:4 ratio | 70.07                    | Real time |

DPPU: Depend on the performance of processing unit.

In addition, the computation power of all-optical networks is currently limited due to the lack of non-linear computing. However, integration with optical non-linear materials, such as magneto-optical traps [52] and photo-refractive crystals [53], provides the possibility to enhance the computation power and further improve the precision of nodule detection and classification. Moreover, as manufacturing processes continue to develop, it may be possible to fabricate an integrated device that can address both nodule detection and classification, provided that non-linear materials can be incorporated into the device.

Hopefully, this approach of using all-optical fast computation devices in medical image real-time processing for aided diagnosis will soon become a reality.

**Table 4.** Comparison with Other Studies in Nodule Classification Task.

| Study                      | Accuracy (%) | Recall (Sensitivity) (%) | Specificity (%) | AUC    | Runtime   |
|----------------------------|--------------|--------------------------|-----------------|--------|-----------|
| Song et al. [41]           | 82.59        | 83.96                    | 81.35           | 0.884  | DPPU      |
| Nibali et al. [47]         | 89.90        | 91.07                    | 88.64           | 0.9459 | DPPU      |
| Zhao et al. [48]           | 82.2         | NA                       | NA              | 0.877  | DPPU      |
| Apostolopoulos et al. [42] | 92.07        | 89.35                    | 94.80           | 0.9208 | DPPU      |
| Ours                       | 76.77        | 65.97                    | 85.85           | 0.8292 | Real time |

DPPU: Depend on the performance of processing unit.

**Author Contributions:** Conceptualization, J.S., L.Z. and W.Z.; methodology, J.S., L.Z. and W.Z.; software, J.S.; validation, L.Z. and W.Z.; formal analysis, L.Z. and W.Z.; investigation, L.Z. and W.Z.; resources, T.L. and X.Y.; data curation, L.Z.; writing—original draft preparation, J.S. and L.Z.; writing—review and editing, S.Y.F.Y. and W.Z.; visualization, W.Z.; supervision, X.Y.; project administration, S.Y.F.Y. and W.Z.; funding acquisition, S.Y.F.Y., W.Z. and X.Y. All authors have read and agreed to the published version of the manuscript.

**Funding:** This research was funded by Guangdong Major Project of Basic and Applied Basic Research, grant number 2020B0301030009; National Natural Science Foundation of China, grant numbers 61935013 and 62005180; Key Research Project of Zhejiang Lab, grant number 2022MG0AC05; Zhejiang Lab Open Research Project, grant number K2022MG0AB01; State Key Laboratory of Advanced Displays and Optoelectronics Technologies (HKUST), grant number ITC-PSKL12EG02; Shenzhen Science and Technology Innovation Commission, grant number 20200806173720001; and Shenzhen Newly Introduced High-End Talents Research Startup Project, grant numbers 827000593 and 827000638.

**Institutional Review Board Statement:** Not applicable.

**Informed Consent Statement:** Not applicable.

**Data Availability Statement:** Data underlying the results presented in this paper are not publicly available at this time but may be obtained from the authors upon reasonable request.

**Acknowledgments:** The authors are very thankful to Guang Li and Yantian Zhang for administrative support.

**Conflicts of Interest:** The authors declare no conflict of interest.

## References

- Vaswani, A.; Shazeer, N.; Parmar, N.; Uszkoreit, J.; Jones, L.; Gomez, A.N.; Kaiser, L.; Polosukhin, I. Attention is all you need. *Adv. Neural Inf. Process Syst.* **2017**, *30*.
- Sutskever, I.; Vinyals, O.; Le, Q.V. Sequence to sequence learning with neural networks. *Adv. Neural Inf. Process Syst.* **2017**, *27*.
- Zhang, T.; Ye, W.; Yang, B.; Zhang, L.; Ren, X.; Liu, D.; Sun, J.; Zhang, S.; Zhang, H.; Zhao, W. Frequency-Aware Contrastive Learning for Neural Machine Translation. In Proceedings of the AAAI Conference on Artificial Intelligence, Online, 22 February 2022.
- Krizhevsky, A.; Sutskever, I.; Hinton, G.E. ImageNet classification with deep convolutional neural networks. *Commun. ACM* **2017**, *60*, 84–90. [[CrossRef](#)]
- Ioffe, S.; Szegedy, C. Batch Normalization: Accelerating Deep Network Training by Reducing Internal Covariate Shift. In Proceedings of the 32nd International Conference on Machine Learning, Lille, France, 6 July 2015.
- He, K.; Zhang, X.; Ren, S.; Sun, J. Deep Residual Learning for Image Recognition. In Proceedings of the 2016 IEEE Conference on Computer Vision and Pattern Recognition, Las Vegas, NV, USA, 27 June 2016.
- Ren, S.; He, K.; Girshick, R.; Sun, J. Faster R-CNN: Towards real-time object detection with region proposal networks. *Adv. Neural Inf. Process Syst.* **2015**, *28*. [[CrossRef](#)] [[PubMed](#)]
- Redmon, J.; Divvala, S.; Girshick, R.; Farhadi, A. You Only Look Once: Unified, Real-Time Object Detection. In Proceedings of the 2016 IEEE Conference on Computer Vision and Pattern Recognition, Las Vegas, NV, USA, 27 June 2016.
- Lin, T.Y.; Dollár, P.; Girshick, R.; He, K.; Hariharan, B.; Belongie, S.J. Feature Pyramid Networks for Object Detection. In Proceedings of the 2016 IEEE Conference on Computer Vision and Pattern Recognition, Las Vegas, NV, USA, 27 June 2016.
- Wang, C.Y.; Bochkovskiy, A.; Liao, H.Y.M. Scaled-YOLOv4: Scaling Cross Stage Partial Network. In Proceedings of the 2021 IEEE/CVF Conference on Computer Vision and Pattern Recognition, Online, 20 June 2021.
- Long, J.; Shelhamer, E.; Darrell, T. Fully Convolutional Networks for Semantic Segmentation. In Proceedings of the 2015 IEEE Conference on Computer Vision and Pattern Recognition, Boston, MA, USA, 7 June 2015.

12. Badrinarayanan, V.; Kendall, A.; Cipolla, R. SegNet: A deep convolutional encoder-decoder architecture for image segmentation. *IEEE Trans. Pattern Anal. Mach. Intell.* **2017**, *39*, 2481–2495. [[CrossRef](#)]
13. Borse, S.; Wang, Y.; Zhang, Y.; Porikli, F. InverseForm: A Loss Function for Structured Boundary-Aware Segmentation. In Proceedings of the 2021 IEEE/CVF Conference on Computer Vision and Pattern Recognition, Online, 19 June 2021.
14. Choi, J.; Chun, D.; Kim, H.; Lee, H.J. Gaussian YOLOv3: An Accurate and Fast Object Detector Using Localization Uncertainty for Autonomous Driving. In Proceedings of the 2019 IEEE/CVF International Conference on Computer Vision, Seoul, Republic of Korea, 27 October 2019.
15. Aghdam, H.H.; Heravi, E.J.; Demilew, S.S.; Laganieri, R. RAD: Realtime and Accurate 3D Object Detection on Embedded Systems. In Proceedings of the 2021 IEEE/CVF Conference on Computer Vision and Pattern Recognition, Online, 20 June 2021.
16. Xu, X.Y.; Tan, M.X.; Corcoran, B.; Wu, J.Y.; Boes, A.; Nguyen, T.G.; Chu, S.T.; Little, B.E.; Hicks, D.G.; Morandotti, R.; et al. 11 TOPS photonic convolutional accelerator for optical neural networks. *Nature* **2021**, *589*, 44–51. [[CrossRef](#)]
17. Jiang, Y.; Zhang, W.J.; Yang, F.; He, Z.Y. Photonic convolution neural network based on interleaved time-wavelength modulation. *J. Light. Technol.* **2021**, *39*, 4592–4600. [[CrossRef](#)]
18. Shen, Y.C.; Harris, N.C.; Skirlo, S.; Prabhu, M.; Baehr-Jones, T.; Hochberg, M.; Sun, X.; Zhao, S.J.; Larochelle, H.; Englund, D.; et al. Deep learning with coherent nanophotonic circuits. *Nat. Photonics* **2017**, *11*, 441–446. [[CrossRef](#)]
19. Hughes, T.W.; Minkov, M.; Shi, Y.; Fan, S.H. Training of photonic neural networks through in situ backpropagation and gradient measurement. *Optica* **2018**, *5*, 864–871. [[CrossRef](#)]
20. Fang, M.Y.S.; Manipatruni, S.; Wierzynski, C.; Khosrowshahi, A.; DeWeese, M.R. Design of optical neural networks with component imprecisions. *Opt. Express* **2019**, *27*, 14009–14029. [[CrossRef](#)]
21. Feldmann, J.; Youngblood, N.; Wright, C.D.; Bhaskaran, H.; Pernice, W.H.P. All-optical spiking neurosynaptic networks with self-learning capabilities. *Nature* **2019**, *569*, 208–214. [[CrossRef](#)] [[PubMed](#)]
22. Xiang, S.Y.; Ren, Z.X.; Song, Z.W.; Zhang, Y.H.; Guo, X.X.; Han, G.Q.; Hao, Y. Computing primitive of fully VCSEL-based all-optical spiking neural network for supervised learning and pattern classification. *IEEE Trans. Neural Netw. Learn. Syst.* **2021**, *32*, 2494–2505. [[CrossRef](#)] [[PubMed](#)]
23. Lin, X.; Rivenson, Y.; Yardimej, N.T.; Veli, M.; Luo, Y.; Jarrahi, M.; Ozcan, A. All-optical machine learning using diffractive deep neural networks. *Science* **2018**, *361*, 1004–1008. [[CrossRef](#)] [[PubMed](#)]
24. Li, J.X.; Mengü, D.; Luo, Y.; Rivenson, Y.; Ozcan, A. Class-specific differential detection in diffractive optical neural networks improves inference accuracy. *Adv. Photonics* **2019**, *1*, 046001. [[CrossRef](#)]
25. Yan, T.; Wu, J.M.; Zhou, T.K.; Xie, H.; Xu, F.; Fan, J.T.; Fang, L.; Lin, X.; Dai, Q.H. Fourier-space diffractive deep neural network. *Phys. Rev. Lett.* **2019**, *123*, 023901. [[CrossRef](#)]
26. Zhou, T.K.; Lin, X.; Wu, J.M.; Chen, Y.T.; Xie, H.; Li, Y.P.; Fan, J.T.; Wu, H.Q.; Fang, L.; Dai, Q.H. Large-scale neuromorphic optoelectronic computing with a reconfigurable diffractive processing unit. *Nat. Photonics* **2021**, *15*, 367–373. [[CrossRef](#)]
27. Rahman, M.S.S.; Li, J.X.; Mengü, D.; Rivenson, Y.; Ozcan, A. Ensemble learning of diffractive optical networks. *Light Sci. Appl.* **2021**, *10*, 14. [[CrossRef](#)]
28. Fang, T.; Li, J.W.; Zhang, X.; Dong, X.W. Classification accuracy improvement of the optical diffractive deep neural network by employing a knowledge distillation and stochastic gradient descent beta-Lasso joint training framework. *Opt. Express* **2021**, *29*, 44264–44274. [[CrossRef](#)]
29. Shi, J.S.; Chen, Y.S.; Zhang, X.Y. Broad-spectrum diffractive network via ensemble learning. *Opt. Lett.* **2022**, *47*, 605–608. [[CrossRef](#)]
30. Mengü, D.; Zhao, Y.F.; Yardimci, N.T.; Rivenson, Y.; Jarrahi, M.; Ozcan, A. Misalignment resilient diffractive optical networks. *Nanophotonics* **2020**, *9*, 4207–4219. [[CrossRef](#)]
31. Mengü, D.; Rivenson, Y.; Ozcan, A. Scale-, shift-, and rotation-invariant diffractive optical networks. *ACS Photonics* **2021**, *8*, 324–334. [[CrossRef](#)]
32. Shi, J.S.; Chen, M.C.; Wei, D.; Hu, C.; Luo, J.; Wang, H.W.; Zhang, X.Y.; Xie, C.S. Anti-noise diffractive neural network for constructing an intelligent imaging detector array. *Opt. Express* **2020**, *28*, 37686–37699. [[CrossRef](#)] [[PubMed](#)]
33. Mengü, D.; Luo, Y.; Rivenson, Y.; Ozcan, A. Analysis of diffractive optical neural networks and their integration with electronic neural networks. *IEEE J. Sel. Top. Quantum Electron.* **2020**, *26*, 1–14. [[CrossRef](#)] [[PubMed](#)]
34. Luo, Y.; Mengü, D.; Yardimci, N.T.; Rivenson, Y.; Veli, M.; Jarrahi, M.; Ozcan, A. Design of task-specific optical systems using broadband diffractive neural networks. *Light Sci. Appl.* **2019**, *8*, 112. [[CrossRef](#)]
35. Veli, M.; Mengü, D.; Yardimci, N.T.; Luo, Y.; Li, J.X.; Rivenson, Y.; Jarrahi, M.; Ozcan, A. Terahertz pulse shaping using diffractive surfaces. *Nat. Commun.* **2021**, *12*, 37. [[CrossRef](#)]
36. Qian, C.; Lin, X.; Lin, X.B.; Xu, J.; Sun, Y.; Li, E.R.; Zhang, B.L.; Chen, H.S. Performing optical logic operations by a diffractive neural network. *Light Sci. Appl.* **2020**, *9*, 59. [[CrossRef](#)]
37. Luo, Y.; Mengü, D.; Ozcan, A. Cascadable all-optical NAND gates using diffractive networks. *Sci. Rep.* **2022**, *12*, 7121. [[CrossRef](#)]
38. Ali, I.; Hart, G.R.; Gunabushanam, G.; Liang, Y.; Muhammad, W.; Nartowt, B.; Kane, M.; Ma, X.M.; Deng, J. Lung nodule detection via deep reinforcement learning. *Front. Oncol.* **2018**, *8*, 108. [[CrossRef](#)]
39. Harsono, I.W.; Liawatimena, S.; Cenggoro, T.W. Lung nodule detection and classification from Thorax CT-scan using RetinaNet with transfer learning. *J. King Saud Univ.-Comput. Inf. Sci.* **2020**, *34*, 567–577. [[CrossRef](#)]
40. Cao, H.C.; Liu, H.; Song, E.M.; Ma, G.Z.; Xu, X.Y.; Jin, R.C.; Liu, T.Y.; Hung, C.C. A two-stage convolutional neural networks for lung Nodule Detection. *IEEE J. Biomed. Health Inform.* **2020**, *24*, 2006–2015. [[CrossRef](#)]

41. Song, Q.Z.; Zhao, L.; Luo, X.K.; Dou, X.C. Using deep learning for classification of lung nodules on computed tomography images. *J. Healthc. Eng.* **2017**, *2017*, 8314740. [[CrossRef](#)] [[PubMed](#)]
42. Apostolopoulos, I.D.; Papathanasiou, N.D.; Panayiotakis, G.S. Classification of lung nodule malignancy in computed tomography imaging utilising generative adversarial networks and semi-supervised transfer learning. *Biocybern. Biomed. Eng.* **2021**, *41*, 1243–1257. [[CrossRef](#)]
43. Chen, H.; Feng, J.A.; Jiang, M.W.; Wang, Y.Q.; Lin, J.; Tan, J.B.; Jin, P. Diffractive deep neural networks at visible wavelengths. *Engineering* **2021**, *7*, 1483–1491. [[CrossRef](#)]
44. Luo, X.H.; Hu, Y.Q.; Ou, X.N.; Li, X.; Lai, J.J.; Liu, N.; Cheng, X.B.; Pan, A.L.; Duan, H.G. Metasurface-enabled on-chip multiplexed diffractive neural networks in the visible. *Light Sci. Appl.* **2022**, *11*, 158. [[CrossRef](#)]
45. Hu, Y.; Fu, S.; Wang, S.; Zhang, W.; Kwok, H.S. Flatness and Diffractive Wavefront Measurement of Liquid Crystal Computer-Generated Hologram Based on Photoalignment Technology. In Proceedings of the 9th International Symposium on Advanced Optical Manufacturing and Testing Technologies: Meta-Surface-Wave and Planar Optics, Chengdu, China, 26 June 2018.
46. Goodman, J.W. *Introduction to Fourier Optics*; Roberts and Company Publishers: Greenwood Village, CO, USA, 2005.
47. Nibali, A.; He, Z.; Wollershhheim, D. Pulmonary nodule classification with deep residual networks. *Int. J. Comput. Assist. Radiol. Surg.* **2017**, *12*, 1799–1808. [[CrossRef](#)]
48. Zhao, X.; Liu, L.; Qi, S.; Teng, Y.; Li, J.; Qian, W. Agile convolutional neural network for pulmonary nodule classification using CT images. *Int. J. Comput. Assist. Radiol. Surg.* **2018**, *13*, 585–595. [[CrossRef](#)]
49. Kulce, O.; Mengu, D.; Rivenson, Y.; Ozcan, A. All-optical information-processing capacity of diffractive surfaces. *Light Sci. Appl.* **2021**, *10*, 25. [[CrossRef](#)]
50. Li, J.; Hung, Y.C.; Kulce, O.; Mengu, D.; Ozcan, A. Polarization multiplexed diffractive computing: All-optical implementation of a group of linear transformations through a polarization-encoded diffractive network. *Light Sci. Appl.* **2022**, *11*, 153. [[CrossRef](#)]
51. Bai, B.; Li, Y.; Luo, Y.; Li, X.; Cetintas, E.; Jarrahi, M.; Ozcan, A. All-optical image classification through unknown random diffusers using a single-pixel diffractive network. *Light Sci. Appl.* **2023**, *12*, 69. [[CrossRef](#)]
52. Zuo, Y.; Li, B.H.; Zhao, Y.J.; Jiang, Y.; Chen, Y.C.; Chen, P.; Jo, G.B.; Liu, J.W.; Du, S.W. All-optical neural network with nonlinear activation functions. *Optica* **2019**, *6*, 1132–1137. [[CrossRef](#)]
53. Li, Y.M.; Zheng, Z.X.; Li, R.; Chen, Q.; Luan, H.T.; Yang, H.; Zhang, Q.M.; Gu, M. Multiscale diffractive U-Net: A robust all-optical deep learning framework modeled with sampling and skip connections. *Opt. Express* **2022**, *30*, 36700–36710. [[CrossRef](#)] [[PubMed](#)]

**Disclaimer/Publisher’s Note:** The statements, opinions and data contained in all publications are solely those of the individual author(s) and contributor(s) and not of MDPI and/or the editor(s). MDPI and/or the editor(s) disclaim responsibility for any injury to people or property resulting from any ideas, methods, instructions or products referred to in the content.